Directional multiscale representations and applications in digital neuron reconstruction

Cihan Kayasandik[b], Kanghui Guo[a], Demetrio Labate[b,*]

[a] *Missouri State University, Department of Mathematics, Springfield, Missouri, USA*
[b] *University of Houston, Department of Mathematics, Houston, Texas, USA*

Abstract

Recent advances in the field of multiscale representations have spurred the emergence of a new generation of powerful techniques for the efficient analysis of images and other multidimensional data. These novel techniques enable the quantification of essential geometric characteristics in complex imaging data resulting in improved algorithms for image restoration, feature extraction and classification. We discuss the application of these ideas in neuroscience imaging and describe a novel method for the accurate and efficient identification of cellular bodies of neurons in multicellular images. This method is instrumental to the design of a novel algorithm for neuronal tracing.

Keywords: fluorescent microscopy, multiscale analysis, neuron profiling, neuron reconstruction, sparse representations, wavelets

2010 MSC: 42C15, 42C40, 92C15, 92C55

1. Introduction

Remarkable advances in fluorescent microscopy during the last decade have created great opportunities for scientific investigation and discovery in neuroscience by enabling fast acquisition of large volumes of high-resolution images. However, to process such data efficiently and take advantage of the wealth of

*Corresponding author
Email addresses: kayasa89@math.uh.edu (Cihan Kayasandik), KanghuiGuo@MissouriState.edu (Kanghui Guo), dlabate@math.uh.edu (Demetrio Labate)

information made available by new technologies, there is not only a need of improved and highly specialized image processing algorithms but also of more targeted and conceptually innovative strategies to interrogate the data.

To address such challenges, a major interdisciplinary effort is being undertaken by the scientific community that brings together ideas from mathematics, statistics and computer science. As a result of this effort, several remarkable initiatives were launched in recent years aimed at tackling specific image processing tasks in the field of neuroscience, including neuron segmentation, cell counting and most prominently digital neuron reconstruction [1, 2, 3, 4, 5]. Digital neuron reconstruction or neuronal tracing requires to automatically reconstruct neuronal morphology in an image by recovering the graph connectivity of the neuronal processes and other shape characteristics (e.g., neurite length, neurite diameter). By tracing neurons and extracting their fundamental morphometric characteristics, researchers can understand neuronal structure and investigate fundamental relationships between shape properties and neuronal function. Because of the complexity of neuron morphology and the low signal-to-noise ratio found in many images, digital neuron reconstruction is among the most difficult tasks in computational neuroscience [6]. Despite the progress made in recent years, significant challenges remain to be solved.

Due to their ability to capture structural information in images, directional multiscale methods emerged in recent years can be very effective in extracting and quantifying critical information from images containing complex structures. The competitive performance of these methods in problems of image denoising and enhancement has been already demonstrated in the literature. The emphasis of this paper is the application of these ideas to quantify morphological properties of neurons through a geometric descriptor called Directional Ratio. We provide a novel theoretical analysis to show that this method precisely quantifies the degree of local anisotropy of indicator functions of planar regions and that this property can be applied to reliably separate neuronal sub-compartments in microscopy images. We next discuss how this method for neuronal segmentation is instrumental to design an innovative algorithm of neuronal tracing. The code

developed by the authors is released open source and freely available.

The rest of the paper is organized as follows. In Sec. 2, we briefly review the application of advanced multiscale representations to process fluorescent images of neurons. In Sec. 3, we analyze the properties of the Directional Ratio and illustrate its application for the separation of somas and dendrites in fluorescent images of neurons. We briefly discuss how our method for the separation of somas and dendrites is applied to designed an improved algorithm for neuron sorting and tracing.

2. Fluorescent image processing

Fluorescent microscopy plays a fundamental role in neuroscience imaging. Spectacular advances in microscopy techniques and fluorescent probes during the last decade have opened remarkable possibilities to monitor neuronal activity even at single-synapse resolution. Thanks to fluorochromes with separable spectral properties and infocus image acquisition from selected depths (e.g., via confocal microscopy) fluorescence imaging enables the simultaneous, multichannel visualization of specific macromolecular constituents of neurons at single cell level and within brain circuits.

However, processing fluorescent images poses particular challenges due to low signal-to-noise ratio, unequal staining as well as the complexity of structures that need to be identified. Such challenges are particularly evident in the problem of neuronal reconstruction where it is required to recover complex structures occurring at various scales, including blob-like and tubular structures.

A variety of ideas of have been applied to the task of neuronal reconstruction as illustrated in recent reviews [4, 6]. Traditional signal processing approaches, e.g., median filters and morphological operators, often perform poorly in processing fluorescent images due to their limitations in recovering edges and dealing with features occurring over multiple scales. To illustrate such challenges, consider a typical confocal image of cultured neurons in Fig. 1. The image shows that the application of intensity thresholding (i.e., the separation of points based

on their pixel intensity) is unable to effectively separate neurons from the background. In addition, it is not effective at separating cell bodies from neurites since high intensity values may occur in both locations. We recall that neurons are the main processing units of the central nervous system. Each neuron consists of a cell body or *soma*, several processes called *dendrites* and one long and thin process called *axon*. The term *neurite* is used to refer to either a dendrite or an axon.

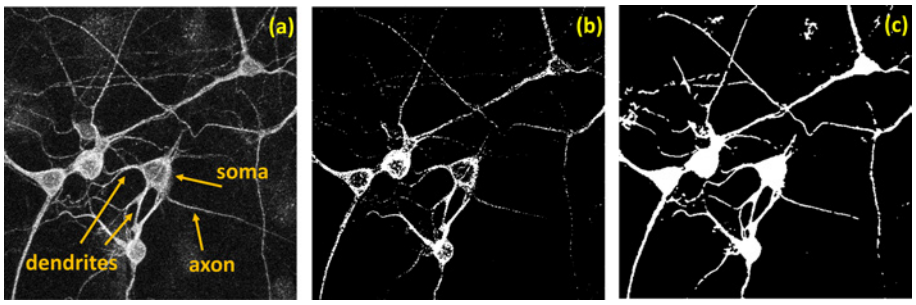

Figure 1: *(a) Confocal image of cultured neurons. Each neuron consists of a soma, several processes called dendrites and one long process called axon. (b) Corresponding intensity thresholded image and (c) segmented image using an SVM approach with shearlet features.*

In Fig. 1(c), we show the segmentation result using a method based on Support Vector Machines (SVM) [7]. This supervised classification method maps data by an embedding to a high dimensional Euclidean space $\mathbb{R}^n$ and through this embedding non-linear separation can be achieved using a linear classifier. Although the implementation of an SVM algorithm is rather simple, very accurate classification can be achieved by building appropriate feature vectors. In the application shown in Fig. 1(c), feature vectors are based on the shearlet tranform of the image (using the frequency-based shearlet filters from [8]) and this choice of feature vectors enables state-of-the-art segmentation performance for segmentation of fluorescent images of neurons. We refer to [9, 10] for details about this approach, its performance and the link to the numerical code.

Below, we briefly recall the main properties of the shearlet framework.

2.1. Sparse image representations by shearlets

Shearlets and curvelets were introduced during the last decade to overcome limitations of traditional multiscale systems in dealing with multidimensional data [11, 12, 13]. Both methods consist of systems of well-localized waveforms defined not only over a range of scales and locations, like wavelets, but also over multiple orientations and with highly anisotropic shapes. Due to their high directional sensitivity, they are especially efficient to approximate edges and other elongated features in images.

In dimension $n = 2$, shearlets are generated by the action of anisotropic dilations and shear transformations on a pair of generator functions $\psi^{(\nu)} \in L^2(\mathbb{R}^2)$, $\nu = 1, 2$, that is,

$$\psi^{(\nu)}_{j,\ell,k}(x) = 2^{3j/2}\psi^{(\nu)}(B^{\ell}_{\nu}A^{j}_{\nu}x - k),$$

for $j \geq 0$, $-2^j \leq \ell \leq 2^j$, $k \in \mathbb{Z}^2$, where $A_1 = \left(\begin{smallmatrix} 4 & 0 \\ 0 & 2 \end{smallmatrix}\right), A_2 = \left(\begin{smallmatrix} 2 & 0 \\ 0 & 4 \end{smallmatrix}\right)$ are the *anisotropic dilation matrices* and $B_1 = \left(\begin{smallmatrix} 1 & 1 \\ 0 & 1 \end{smallmatrix}\right), B_2 = B_1^t$ are the *shear matrices* (see [14] for details). Hence the indices j, ℓ, k are associated with a range of scales, orientations and locations, respectively. Curvelets have a different and slightly more involved construction that involves anisotropic dilations, rotations and (non-integer) translations [11].

By combining multiscale analysis and high directional sensitivity, shearlets and curvelets provide highly sparse representations for a large class of multidimensional data, outperforming conventional wavelets. One can prove that shearlets or curvelets provide optimally sparse approximations in the model class of carton-like functions outperforming wavelet-based approximations [11, 15]. Sparsity has implications not only for image restoration [8, 16, 17, 18] since finding a sparse representation of an image usually entails capturing its dominant structures. As a result, shearlet-based features were recently employed to identify and quantify geometric characteristics in fluorescent images of neurons including the quantification of neurite orientations [19] and the segmentation of neurons [20].

In the next section, we discuss a method for neuronal reconstruction adapting ideas from the framework of directional multiscale representations.

3. Segmentation of fluorescent images of neurons

We consider here the problem of segmenting images of neurons containing multiple cells and identifying their main sub-compartments, namely somas and neurites. A related problem is to sort individual neurons in the image by automatically assigning each neurite to the respective cell. We will focus first on the easier task of finding and segmenting each soma in the image. We will discuss next how this is used to address the sorting and tracing problem.

Automated segmentation of somas in fluorescent images of neurons such as Fig. 1 can be challenging due to the lack of selective markers and that large variability in shape and size. In fluorescent images of neurons, somas are usually visualized in the channel marked by the MAP2 (microtubules associated protein 2) antibody staining which is diffusely distributed in both somas and dendrites. While it is also possible to use a marker to visualized the cell nucleus, this organ occupies only a relatively small region inside the soma so that also in this case further processing is needed to separate somas from neurites.

The simplest method for separating the two structures is to threshold the image based on intensity values [21, 22]. However this approach is unreliable since high-intensity regions are frequently found outside somas as shown in Fig. 1. Algorithms based on morphological operators perform generally better but are very sensitive to parameter setting (e.g., size of structuring elements) [23, 24] and their performance may decrease significantly when images contain multiple cells and possibly clustered somas [25]. Methods based on machine learning were also proposed [26] but they require a training stage, making their implementation computationally more involved and more sensitive to the specific neuronal subpopulation on which they are trained. To overcome such limitations, the authors of this paper have recently introduced a new geometric descriptor called Directional Ratio that relies on the geometric notion of *local isotropy* [27]. This

method consists in applying this geometric descriptor to a segmented image of neurons in order to separate somas from neurites and is illustrated in Sec. 3.4. Numerical studies by the authors in [25] have shown that this method performs very competitively against other algorithms. Here we provide a proof of concept of this new method using a simplified mathematical model.

Definition 1. *A point x in a region A is a point of isotropy of A at scale s if there is a ball of radius $s/2$ centered at x which is entirely contained in A.*

Intuitively, in an image containing blob-like and vessel-like regions, we expect to find a range of scales such that the points of local isotropy points are located precisely inside the blob-like regions. Hence, somas and neurites could be separate based on the local isotropy calculated over an appropriate range of scales.

3.1. Directional Ratio and soma detection

The Directional Ratio was introduced as an algorithmic and practical method to identify points in an image based on local isotropy properties [10]. For its definition, we need to consider a collection of *multiscale directional filters*, that is, an appropriate set of functions $\{\phi_{a,\theta} : a > 0, \theta \in [0,\pi)\} \subset L^2(\mathbb{R}^2)$, where a is a scale parameter and θ is a directional parameter. Hence the *Directional Ratio of a function $f \in L^2(\mathbb{R}^2)$ at scale a and location $p \in \mathbb{R}^2$* is defined as

$$D_a f(p) = \frac{\min_{\theta\in[0,\pi)}\{|f * \phi_{a,\theta}(p)|\}}{\max_{\theta\in[0,\pi)}\{|f * \phi_{a,\theta}(p)|\}}, \tag{1}$$

where

$$f * \phi_{a,\theta}(p) = \int_{\mathbb{R}^2} f(x)\, \phi_{a,\theta}(p-x)\, dx \tag{2}$$

is the convolution of f and $\phi_{a,\theta}$. Note that $D_a f$ takes values in $[0,1]$.

In a nutshell, the function $D_a f(p)$ quantifies the degree of isotropy of f at a location p and scale a by taking the ratio of the smallest directional filter response vs the largest one. If the filter response at p is independent of the direction, then $D_a f(p) = 1$; this indicates that p is a point of local isotropy of

f at scale a. Points p for which $D_a f(p) < 1$ correspond to locations with a lack of isotropy at scale a - the closer to 0, the higher the anisotropy.

A very simple choice of filters consists in taking rotated and rescaled versions of a rectangular window. That is, let $\phi = \chi_Q$, where Q is the rectangle $[-L/2, L/2] \times [-1/2, 1/2]$, for a fixed parameter $L \geq 1$. Next we define the *multiscale directional rectangular filters* $\phi_{a,\theta} = \Delta_a R_\theta \phi$, where R_θ denotes the 2D rotation by an angle $(-\theta)$ and Δ_a is the (anisotropic) dilation operator $\Delta_a f(x_1, x_2) = a^{-\frac{1+\alpha}{2}} f(a^{-1}x_1, a^{-\alpha}x_2)$, for a fixed $\alpha \in (0, 1]$; the parameter α controls the anisotropy of the scaling being applied (no anisotropy for $\alpha = 1$, increasingly more anisotropy as α approaches 0). That is, the filter $\phi_{a,\theta}$ is the indicator function of the oriented rectangular window $Q_{a,\theta}$ obtained by rescaling Q by a along the x direction and by a^α along the y direction, and next rotating the resulting rectangle by θ. In this case, the convolution (2) becomes simply the integration

$$f * \phi_{a,\theta}(p) = \int_{Q^p_{a,\theta}} f(x)\, dx,$$

where $Q^p_{a,\theta}$ denotes the rectangle $Q_{a,\theta}$ centered at p.

To assess the theoretical performance of the Directional Ratio for separating regions of different local isotropy, we examine below its application where f is the characteristic of a region including (i) a disk and (ii) a long and thin rectangle - an assumption that makes the analytic computation of (1) easier. This choice of f is meant as an idealized model of the image of a cell body and a vessel. While cell bodies found in experimental images can be more elongated and vessels not necessarily straight, we will show that the predictions of the theorem hold remarkably well in typical fluorescent images of neurons.

Theorem 1. *Let $f = \chi_{S \cup N}$ where S is a disk of radius $R > 0$ and N is a rectangle of infinite length and width w, where $S \cap N = \varnothing$. Let the Directional Ratio be given by* (1) *with the multiscale directional rectangular filters $\phi_{a,\theta}$ defined as above.*

(a) Assume $L \geq 2w$. Then, for any $p \in N$, provided that $a > 4w/L$ and $a^{1-\alpha} > 4/L$, it follows that $D_a f(p) < 1/2$.

(b) There exists a range of scales such that for all points p inside the disk of radius $0.65R$ concentric with S we have $D_a f(p) > 1/2$.

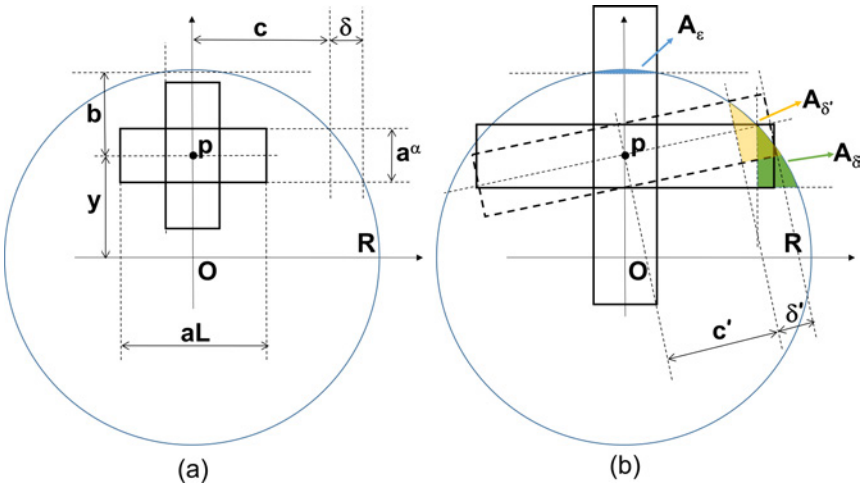

Figure 2: Computation of the Directional Ratio of the characteristic function of a disk of radius R and center O at $p = (0, y)$. (a) At small scales, when $\frac{aL}{2} \leq b$ (case 1 in narrative), any oriented rectangle $Q_{a,\theta}$ is contained inside the disk (here we show two rectangles at scale a and orientations $\theta = 0, \pi/2$). (b) At larger scales, $c < \frac{aL}{2} \leq 2c - b$ (case 3 in narrative), the area of the region of overlap of the disk and $Q_{a,\theta}$ depends on θ.

PROOF. (a) Without loss of generality, suppose that the rectangle N is centered at the origin, with the long axis parallel to the x_2 coordinate. We start by observing that

$$D_a f(p) \leq \frac{|f * \phi_{a,0}(p)|}{|f * \phi_{a,\pi/2}(p)|} = \frac{\int_{Q^p_{a,0} \cap N} dx}{\int_{Q^p_{a,\pi/2} \cap N} dx}. \tag{3}$$

We consider first the numerator in (3) and the rectangle $Q^p_{a,0}$ associated with the filter $\phi_{a,0}$. Since $L \geq 2w$, the integral $\int_{Q^p_{a,0} \cap N} dx$ is the same for any $p \in N$; that is, $\int_{Q^p_{a,0} \cap N} dx = wa^\alpha$. For the denominator in (3), we observe that the integral $\int_{Q^p_{a,\pi/2} \cap N} dx$ depends on the value of the first coordinate of p. Its value is minimized when $p = (w/2, x_2)$ (i.e., p at the boundary of N), in which case $\int_{Q^p_{a,\pi/2} \cap N} dx = \frac{a^\alpha}{2} aL$. If $a^\alpha \leq w$ (width of filter less or equal than w), using

the assumption that $a > 4w/L$, it follows that, for any $p \in N$

$$D_a f(p) \leq \frac{wa^\alpha}{\frac{a^\alpha}{2}aL} = \frac{2w}{aL} < \frac{1}{2}.$$

Otherwise, if $a^\alpha > w$ (width of filter larger than w), $\int_{Q^p_{a,\pi/2}\cap N} dx \geq \frac{w}{2}aL$ so that, using the assumption that $a^{1-\alpha} > 4/L$, we have

$$D_a f(p) \leq \frac{wa^\alpha}{\frac{w}{2}aL} = \frac{2a^\alpha}{aL} < \frac{1}{2}.$$

(b) Without loss of generality, let us assume that the disk S is centered at the origin and p is located on the vertical axis, i.e., $p = (0, y)$, $0 \leq y \leq 0.65R$. Also, let us assume $a^\alpha \leq \frac{1}{5}R$. We can write

$$D_a f(p) = \frac{\min_{\theta\in[0,\pi)} \int_{Q^p_{a,\theta}\cap S} dx}{\max_{\theta\in[0,\pi)} \int_{Q^p_{a,\theta}\cap S} dx}. \tag{4}$$

If p is at the origin, i.e., $y = 0$, then $\int_{Q^p_{a,\theta}\cap S} dx$ is independent of θ and hence from (4) we observe that $D_a f(p) = 1$. If p is not at the origin, then let b and c be given as in Fig. 2(a); that is, they denote the half-length of the longest vertical and horizontal rectangles, respectively, centered at p and fully contained inside the disk. We discuss below several cases. Note that, since $y \leq 0.65R$ and $R > 5a^\alpha$, it follows that $b > a^\alpha$.

Case 1. $\frac{aL}{2} \leq b$. Note that $b \leq c$. Hence the rectangles $Q^p_{a,\theta}$ of length L are fully contained inside S for all orientations θ; hence $D_a f(p) = 1$.

Case 2. $b < \frac{aL}{2} \leq c$. Since $b \leq c$, the integral $\int_{Q^p_{a,\theta}\cap S} dx$ is maximal when $\theta = 0$ and minimal when $\theta = \pi/2$. We denote by A_ϵ the area of the circular segment whose lower boundary is the line $x_2 = b$ and the upper boundary is the boundary of the disk S (see Fig. 2(b)). Hence

$$D_a f(p) = \frac{(b + \frac{aL}{2})a^\alpha + A_\epsilon}{Laa^\alpha} = \frac{b}{La} + \frac{1}{2} + \frac{A_\epsilon}{Laa^\alpha} > \frac{1}{2}.$$

Case 3. $c < \frac{aL}{2} \leq 2c - b$. The integral $\int_{Q^p_{a,\theta}\cap S} dx$ is still minimal when $\theta = \pi/2$ while the maximal response occurs for an angle $0 \leq \bar{\theta} < \pi/2$.

We consider first the case where $\bar{\theta} = 0$. Denoting by A_δ the area of region of intersection of the rectangle $Q^p_{a,0}$ and the disk S for $x_1 > c$ (see Fig. 2(b)) we

have

$$D_a f(p) = \frac{(b + \frac{aL}{2})a^\alpha + A_\epsilon}{2ca^\alpha + 2A_\delta}.$$

Next we observe that $A_\delta < \delta a^\alpha$, where $\delta = \sqrt{R^2 - (y - \frac{a^\alpha}{2})} - \sqrt{R^2 - (y + \frac{a^\alpha}{2})}$. We can estimate δ as

$$\delta \leq \frac{2ya^\alpha}{\sqrt{R^2 - (y - \frac{a^\alpha}{2})} + \sqrt{R^2 - (y + \frac{a^\alpha}{2})}} \leq \frac{2ya^\alpha}{2\sqrt{R^2 - (y + \frac{a^\alpha}{2})}} = \frac{ya^\alpha}{c}.$$

From the last observation, using the fact that $b > a^\alpha$ and $2c < aL$, it follows that

$$D_a f(p) \geq \frac{(b + \frac{aL}{2})a^\alpha}{2ca^\alpha + 2\frac{ya^\alpha}{c}a^\alpha} = \frac{1}{2}\,\frac{2b + aL}{2c + 2\frac{y}{c}a^\alpha} > \frac{1}{2}\,\frac{aL + 2a^\alpha}{aL + 2\frac{y}{c}a^\alpha}. \tag{5}$$

Let $y = \beta R$, with $0 < \beta \leq 1$. Observe that $R^2 = (y + \frac{a^\alpha}{2})^2 + c^2$ so that $c^2 = R^2 - (y + \frac{a^\alpha}{2})^2$. Hence we can write

$$\frac{y^2}{c^2} = \frac{\beta^2 R^2}{(1 - \beta^2)R^2 - \beta R a^\alpha - \frac{a^{2\alpha}}{4}} \leq \frac{\beta^2 R^2}{(1 - \beta^2)R^2 - \frac{\beta}{5}R^2 - \frac{1}{100}R^2} = \frac{\beta^2}{\frac{99}{100} - \beta^2 - \frac{\beta}{5}}.$$

The above quantity is less than one if $\beta < 0.65$. Hence, using the observation that $\frac{y}{c} < 1$ in (5), it follows that $D_a f(p) > \frac{1}{2}$.

If $\bar{\theta} \neq 0$, then either the rectangle $Q^p_{a,\bar{\theta}}$ overlaps the boundary of the disk at both ends or one of the two ends is fully contained inside the disk. In the first case, the same estimate used in (5) will imply that $D_a f(p) > \frac{1}{2}$. In the second case, we have

$$D_a f(p) = \frac{(b + \frac{aL}{2})a^\alpha + A_\epsilon}{(c' + \frac{aL}{2})a^\alpha + A_{\delta'}},$$

where c' and $A_{\delta'}$ are shown in Fig. 2(b). Since $c' < \frac{aL}{2}$ and $A_{\delta'} \leq A_\delta$, arguing as above we have

$$D_a f(p) \geq \frac{(b + \frac{aL}{2})a^\alpha}{aLa^\alpha + A_\delta} = \frac{1}{2}\,\frac{2b + aL}{aL + \frac{y}{c}a^\alpha} > \frac{1}{2}\,\frac{aL + 2a^\alpha}{aL + \frac{y}{c}a^\alpha} > \frac{1}{2}.$$

Remark 1. The analysis of part (b) of Theorem 1 can be carried over for larger values of a but the detailed discussion would become very technical. We note that, for 'very large' values of a, approximately if $aL > 4R - 2b$, no rectangles

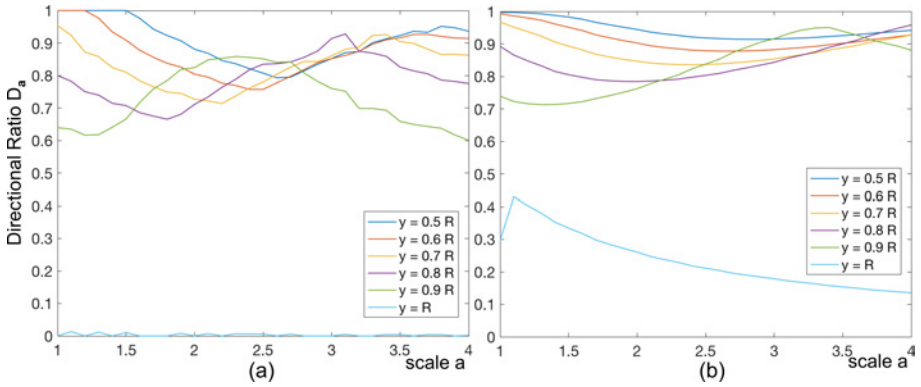

Figure 3: Numerical estimation of the Directional Ratio $D_a f(p)$ as a function of the scale a (measured in pixels) where f is the characteristic function of a disk of radius R centered at O. We display the result for several locations $p = (0, y)$ where $0.5R \leq y \leq R$ using (a) rectangular filters and (b) anisotropic Gaussian filters. As predicted by Theorem 1 and 2, away from the boundary of the disk the values of $D_a f(p)$ is above $\frac{1}{2}$ for a range of scales. To generate these plots we set $R = 200$, $L = 130$ and $H = 33$ pixels.

$Q^p_{a,\theta}$ is contained in S and the directional ratio becomes a constant function of a, namely

$$D_a(p) = \frac{\int_{Q^p_{a,0} \cap S} dx}{\int_{Q^p_{a,\pi/2} \cap S} dx} \approx \frac{c}{R}.$$

We also remark that the value of y in the proof of Theorem 1(b) such that $D_a f(p) > \frac{1}{2}$ can be made larger than $0.65R$ even though one cannot get too close to R. If p is selected very close to the boundary of S, the value of $D_a f(p)$ can become very small. Figure 3(a) displays the values of Directional Ratio computed on a synthetic image $f = \chi_S$ where S is a disk of radius R centered at the origin, as a function of the scale, for representative locations p. The figure shows that the behavior is consistent with the theoretical prediction and that there exists a range of scales such $D_a(p) > \frac{1}{2}$ even for p close to the boundary.

Remark 2. As mentioned above, Theorem 1 is motivated by the problem of separating neurites from somas in microscopy images. Let us be more specific about the dimensions found in typical experimental images.

In a primary rat hippocampal neuron – a frequent animal model – a soma is typically between 10 and 20 μm in diameter, while neurites have diameters between 0.5 and 1.5 μm [28, 29]. Hence in a typical confocal fluorescent image such as Figure 1, where resolution is about 0.25 μm per pixel, a soma is about 40 to 80 pixels in diameter and a neurite is about 2 to 6 pixels in diameter.

Below we verify that the assumptions of Theorem 1 are satisfied in typical images of neurons and show that we can find a range of scales where the computed values of the Directional Ratio separate somas from neurites. For simplicity, we assume that $\alpha = 1/2$.

Based on the dimensions indicated above, we model a neurite as a long rectangle of width $w = 6$. Hence, by choosing $L = 13$ the assumption of Theorem 1(a) is satisfied and $D_a f(p) < 1/2$ for $a > 24/13$. Next we model a soma as a disk S of radius $R = 20$. According to Theorem 1(b), we need to impose $\sqrt{a} \leq \frac{R}{5}$, that is, $a \leq 4$. Hence, for $y = 0.65R$, we find that $b \approx 0.35R$, $c \approx 0.76R$ so that Case 1 holds for $a \leq 1.08$, Case 2 holds for $1.08 < a \leq 2.34$ and Case 3 holds for $2.34 < a \leq 3.60$. For $y = 0.50R$, we find that $b \approx 0.50R$, $c \approx 0.87R$ so that Case 1 holds for $a \leq 1.54$, Case 2 for $1.54 < a \leq 2.68$, Case 3 for $2.68 < a \leq 3.82$.

3.2. Multiscale anisotropic Gaussian filters

There are other choices of directional filters in (1) offering other potential advantages. An important example are the oriented anisotropic Gaussian functions – a class of functions originally introduced for problems of edge detection [30]. They are obtained by scaling a 2D Gaussian using different factors σ_1 and σ_2 in the x_1 and x_2 directions, respectively, as

$$g_0(x_1, x_2; \sigma_1, \sigma_2) = \frac{1}{2\pi\sigma_1\sigma_2} \exp\left(-\frac{1}{2}\left(\frac{x_1^2}{\sigma_1^2} + \frac{x_2^2}{\sigma_2^2}\right)\right),$$

and next rotating the coordinate axes by an angle θ, obtaining:

$$g_\theta(x_1, x_2; \sigma_1, \sigma_2) = \frac{1}{2\pi\sigma_1\sigma_2} \exp\left(-\frac{1}{2}\left(\frac{(x_1\cos\theta + x_2\sin\theta)^2}{\sigma_1^2} + 54\frac{(-x_1\sin\theta + x_2\cos\theta)^2}{\sigma_2^2}\right)\right).$$

One of the most useful properties of these functions is the existence of a very efficient numerical algorithm to implement their convolution in a separable form [31]. That is, the convolution with the anisotropic Gaussian $g_\theta(x_1, x_2; \sigma_1, \sigma_2)$ can be expressed as the composition of a 1D convolution with a Gaussian filter in the x_1 direction followed by another 1D convolution with a Gaussian filter in a non-orthogonal direction, namely:

$$g_\theta(x_1, x_2; \sigma_1, \sigma_2) = \frac{1}{2\pi\sigma_1\sigma_\phi} \exp\left(-\frac{1}{2}\frac{x_1^2}{\sigma_1^2}\right) * \exp\left(-\frac{1}{2}\frac{t^2}{\sigma_\phi^2}\right),$$

where $t = x_1 \cos\phi + x_2 \sin\phi$ and ϕ is an appropriate functions of θ. We remark that this property does not hold in the case of rotated rectangular filters since these functions are not separable except for very special angles of rotation. Additionally, one can implement a convolution with a Gaussian using a recursive approximation. Using these observations one obtains a convolution algorithm that is numerically accurate and significantly faster than a FFT-based 2D convolution[1] In [25], the authors of this paper have adapted this idea to obtain a very fast algorithm for the computation of the Directional Ratio. In particular, they have shown that, for a typical image of 512×512 pixels, the computing time of the algorithm for soma detection based on the Directional Ratio is reduced of about a factor of 4 when the 2D convolution of rectangular filters is replaced by the separable convolution of Gaussian filters (going from 0.86s to 0.21s using a MacBook with Intel Core i5 2.4GHz processor and 16 GB RAM). Using this routine, we can detect somas faster than using standard morphological operators and with much higher accuracy.

Theorem 1 can be carried over to the case of anisotropic Gaussian filters yielding a similar result. In the statement below, we set $\sigma_2 = a$, where $a > 0$ is the scale variable and set $\sigma_1 = H\sigma_y = H = a$, where $H > 1$ is a fixed parameter. We display the plot of the Directional Ratio as a function of the

[1]For an image of size $N \times N$, convolution implemented by FFT requires $\log N^2$ multiplications per pixel; separable convolution requires only $4L$ multiplications per pixel, where $L \times L$ is the filter size; separable convolution and recursive approximation improves further [31].

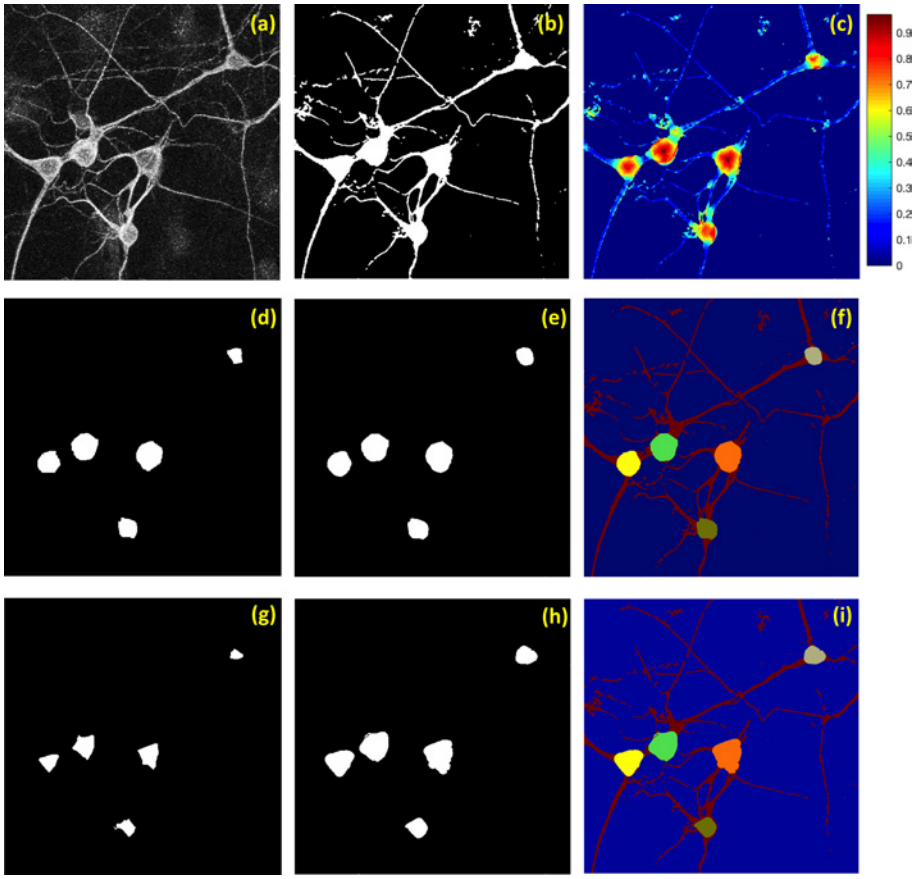

Figure 4: Soma segmentation using Directional Ratio. (a) Confocal image of cultured neurons stained with soma-dendritic (MAP2) marker. Image size 512×512 pixels (1 pixel = 0.25 μm) (b) Segmented binary image. (c) Directional Ratio computed inside the segmented region (white region in Panel B) with values between 0 and 1. For this computation: $a = 2$, $L = 24$. Soma region is obtained by thresholding the Directional Ratio with threshold 0.5 (d) and next applying the Level Set method (e). Computation is repeated by thresholding the Directional Ratio with threshold 0.9 (g) and applying the Level Set method (H). Segmented somas overlapping the segmented image for the two runs of the algorithm are shown in (f) and (i).

scale using anisotropic Gaussian filters in Figure 3(b).

Theorem 2. *Let $f = \chi_{S\cup N}$ where S is a disk of radius $R > 0$ and N is a rectangle of infinite length and width w, where $S \cap N = \varnothing$. Let the Directional Ratio be given by* (1) *with the multiscale anisotropic Gaussian filters $\phi_{a,\theta}(x_1, x_2) = g_\theta(x_1, x_2; aH, a)$.*

(a) Let $M > 0$. For any $p \in N$, if $Ma \le w \le a$, provided $H > M/0.4$ it follows that $D_a f(p) < 1/2$.

(b) Let $H < 40$. There exists a range of scales such that for all points p inside the disk of radius $0.65R$ concentric with S we have $D_a f(p) > 1/2$.

Proof. The proof follows the main ideas of Theorem 1. In a nutshell we will approximate the anisotropic Gaussian function $g_0(x_1, x_2; aH, a)$ with the characteristic function of the rectangle $4aH \times 4a$. In the following, it may be convenient at times to write

$$\phi_{a,0}(x_1, x_2) = g_0(x_1, x_2; aH, a) = \gamma(x_1, aH)\,\gamma(x_2, a),$$

where $\gamma(x_1, \sigma) = \frac{1}{\sqrt{2\pi}\sigma} \exp(-\frac{x_1^2}{2\sigma^2})$.

(a) Without loss of generality, suppose that the rectangle N is centered at the origin, with the long axis parallel to the x_2 coordinate. We start by observing that

$$D_a f(p) \le \frac{|f * \phi_{a,0}(p)|}{|f * \phi_{a,\pi/2}(p)|} = \frac{\int_N \phi_{a,0}(x-p)\,dx}{\int_N \phi_{a,\pi/2}(x-p)\,dx}. \tag{6}$$

The numerator in (6) is maximized when p is on the x_2 axis and the denominator is minimized when p is on the boundary of the set N; without loss of generality, we can choose $p = (0, 0)$ for the numerator and $p = (-w, 0)$ for the denominator.

Hence

$$\begin{aligned} D_a f(p) &\leq \frac{\int\int_N \gamma(x_1, aH)\,\gamma(x_2, a)\,dx_1\,dx_2}{\int\int_N \gamma(x_1+w, a)\,\gamma(x_2, aH)\,dx_1\,dx_2} \\ &= \frac{\int_{-w/2}^{w/2} \gamma(x_1, aH)\,dx_1}{\int_0^w \gamma(x_1, a)\,dx_1} \\ &= 2\,\frac{\int_0^{w/2} \gamma(x_1, aH)\,dx_1}{\int_0^w \gamma(x_1, a)\,dx_1} \\ &= 2\,\frac{\int_0^{w/2H} \gamma(x_1, a)\,dx_1}{\int_0^w \gamma(x_1, a)\,dx_1}. \end{aligned}$$

Using the assumption that $Ma \leq w \leq a$ and that $M < 0.4H$ we conclude that

$$D_a f(p) \leq 2\,\frac{\int_0^{aM/2H} \gamma(x_1, a)\,dx_1}{\int_0^a \gamma(x_1, a)\,dx_1} < \frac{1}{2}.$$

(b) Without loss of generality, we assume that the disk S is centered at the origin and p is located on the vertical axis, i.e., $p = (0, y)$, $0 \leq y \leq 0.65R$. We also assume $R > 20a$ (note: $R > 5(4a)R$ and compare with $R > 5a^\alpha$ in Theorem 1). We can write

$$D_a f(p) = \frac{\min_{\theta\in[0,\pi)} \int_S \phi_{a,\theta}(x-p)\,dx}{\max_{\theta\in[0,\pi)} \int_S \phi_{a,\theta}(x-p)\,dx}. \tag{7}$$

If p is at the origin then $\int_S \phi_{a,\theta}(x-p)\,dx$ is independent of θ and from (7) it follows that $D_a f(p) = 1$. If p is not at the origin, then let b and c denote the half-length of the longest vertical and horizontal rectangles, respectively, of width $4\sigma_2 = 4a$ centered at p and fully contained inside the disk. With this understanding, one can interpret Fig. 2 as illustrating the essential support of the anisotropic Gaussian function, that is, the support accounting of about 95% of its area.

We discuss below several cases. Note that, since $y \leq 0.65R$ and $R > 20a$, it follows that $b > 4a$.

Case 1. $2aH \leq b$. We have

$$D_a f(p) = \frac{\int_S \phi_{a,\pi/2}(x-p)\,dx}{\int_S \phi_{a,0}(x-p)\,dx} \geq \int_S \phi_{a,\pi/2}(x-p)\,dx = \int_{S+p} \phi_{a,\pi/2}(x)\,dx > 0.9,$$

where the last inequality is due to the fact the region of integration $S+p$ contains the rectangle $[-2a, 2a] \times [-2aH, 2aH]$ (recall that $\sigma_2 = a, \sigma_1 = aH$).

Case 2. $b < 2aH \leq 2c$. Since $b \leq c$, again the integral $\int_S \phi_{a,\theta}(x-p)\,dx$ is maximal when $\theta = 0$ and minimal when $\theta = \pi/2$ so that

$$D_a f(p) = \frac{\int_S \phi_{a,\pi/2}(x-p)\,dx}{\int_S \phi_{a,0}(x-p)\,dx} \geq \int_S \phi_{a,\pi/2}(x-p)\,dx = \int_{S+p} \phi_{a,\pi/2}(x)\,dx.$$

Since $b > 4a$ and $2aH \leq 2c$ then the rectangle $[-2a, 2a]\times[-2aH, 4a]$ is contained in the region of integration $S + p$. Since $2La = 2\sigma_1$ and $H \leq 40$, then $4a > 0.1Ha = 0.1\sigma_1$ and $\int_{S+p} \phi_{a,\pi/2}(x)\,dx > 1/2$.

For $2aH > 2c$ the integral $\int_S \phi_{a,\theta}(x-p)\,dx$ is still minimal when $\theta = \pi/2$ while the maximal response occurs for an angle $0 \leq \bar{\theta} < \pi/2$. As a increases further, however, the angle of maximal response becomes $\theta = \pi/2$ and the angle of minimal response $\theta = 0$. In fact, for $2aH \gg R$ and p inside S, we can think $\phi_{a,0}(x-p)$ and $\phi_{a,\pi/2}(x-p)$ as essentially constant along the lines $x_2 = y$ and $x_1 = 0$ respectively. As in theorem 1, for $2aH \gg R$ we will find that $D_a(p) \approx \frac{c}{R}$.

3.3. Effect of noise

So far we have analyzed the computation of the Directional Ratio in the absence of noise. If the image f is corrupted by noise, the value of the Directional Ratio might be affected due to the impact of noise on the convolution $|f * \phi_{a,\theta}|$ that could potentially modify the angle θ at which this quantity attains its maximum or minimum. We argue below that the effect of the noise is not expected to be significant because the convolution with a Gaussian (or rectangular) kernel has the effect of reducing the impact of the noise in the image.

Let us examine the situation where a digital image $f(i, j)$ with values $i, j \in N \times N$ is corrupted by additive white Gaussian noise, that is, at each pixel (i, j), we observe the values

$$f_n(i, j) = f(i, j) + n(i, j)$$

where the noise $n(i, j)$ is i.i.d. with zero mean and standard deviation σ_n.

If ϕ is a Gaussian kernel of standard deviation h, the standard deviation of the noise in $f_n \to f_n * \phi$ is reduced. Namely, let the number of samples k of the noise in an interval of size h be $k = h/\delta$. Then one can show that the

standard deviation of the noise (that can be interpreted as the noise amplitude) is multiplied by $\frac{1}{k\sqrt{8\pi}}$ (cf. Theorem 2.2 in [32]).

Figure 5 shows that the effect of additive white Gaussian noise on the estimation of the Directional Ratio is negligible even for relatively high values of the standard deviation of the noise. Tests run using Poisson noise (not reported here) show that also in that case the impact is negligible.

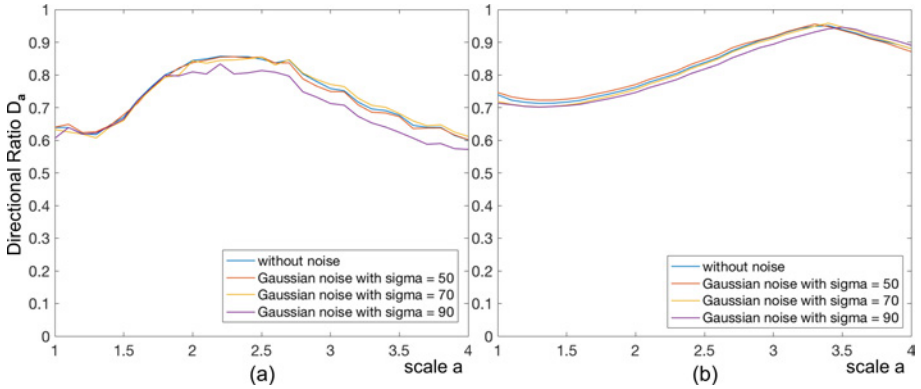

Figure 5: Numerical estimation of the Directional Ratio $D_a f$ at $p = (0, 0.9R)$, as a function of the scale a measured in pixels, in the presence of noise using (a) Rectangular and (b) Anisotropic Gaussian filters. The characteristic function f of the disk of radius R centered at O with amplitude 255 is corrupted by white Gaussian noise with standard deviation $\sigma = 50, 70, 90$. Values of R, L, H are set as in Fig. 3.

3.4. Soma segmentation and neurite separation

As described above, the evaluation of the Directional Ratio of an image is designed to provide quantitative information useful to separate blob-like regions from vessel-like structures. A direct application of this idea to separate somas from neurites in an image of a neurons is illustrated in Fig. 4 and consists of the following steps.

1. *Segmentation.* The image is first segmented using the SVM method discussed in Sec. 2 (Fig. 4(b)). This method generates a binary image identifying a region that contains both somas and neurites.

2. *Directional Ratio.* Directional Ratio is computed at an appropriate scale using as a mask the segmented region computed in step 1 (Fig. 4(c)).
3. *Thresholding.* The Directional Ratio plot is thresholded using as threshold value $\frac{1}{2}$ hence identifying a region corresponding to somas and a complementary region corresponding to neurites (Fig. 4(d)).

As the figure shows, the method based on the Directional Ratio finds the somas in the image very reliably. In addition, thanks to the fast implementation of the anisotropic Gaussian filters, the computing time is faster than standard morphological operators [25]. This implementation has however some limitations due to the simplifying assumptions of our model. In experimental images, somas are not necessarily circular but may be rather elongated with irregular boundaries. To improve the algorithm, a relatively simple refinement consists in the following modification. Following step 3, possibly with a higher threshold value (resulting in the detection of a smaller region as shown in Fig. 4(g)), we apply the classical Level Set algorithm [33] to grow the detected region with a growth speed controlled by the Directional Ratio. The final result displayed in Fig. 4(h-i) shows that this refined version of the algorithm segments the somas with high accuracy. Extensive numerical demonstration of this algorithm including a comparison with competing algorithms can be found in [25]; the numerical code is available at `https://github.com/cihanbilge/SomaExtraction`.

We remark that the selection of the scale parameter at which to compute the Directional Ratio can be automatized by estimating the 'dominant scale' of the image using the principles of automated scale selection [25, 34].

3.5. Digital neuron reconstruction

As observed in Sec. 1, despite the significant progress made by the scientific community, digital neuron reconstruction remains a challenging problem and existing algorithms have still significant limitations. In particular, even though there are tracing algorithms that perform competitively, they are typically designed to process images containing single neurons or multiple neurons that are separated [6, 35, 36]. If multiple cells with non-separated neurons are present,

these methods are usually unable to automatically sort traces into neuronal arbors corresponding to individual neurons [37]. As shown in Fig. 4, even in images of neuronal cultures with relatively low density it is common to see neurites that appear to overlap. Automatically sorting neuronal trees in these images is not a trivial problem in general.

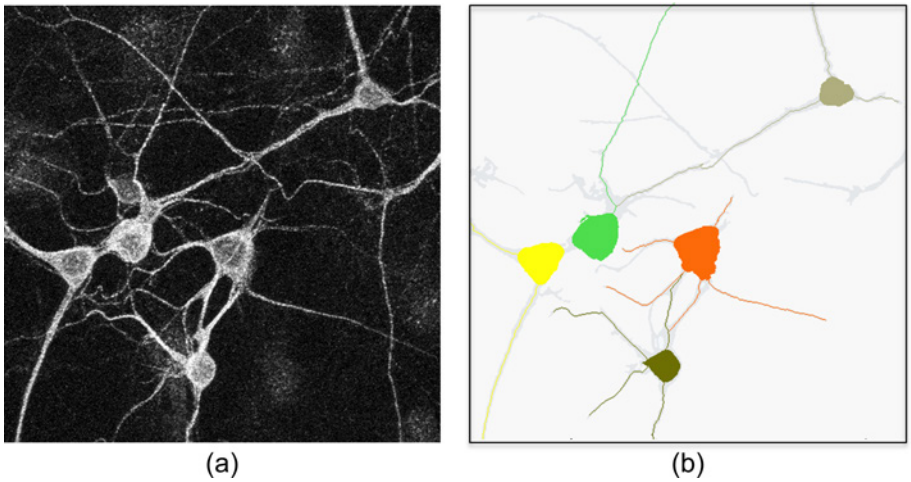

Figure 6: *Neuronal tracing. (a) Confocal image of cultured neurons labelled with anti-MAP2 antibody and (b) corresponding digital reconstruction where somas are segmented and separate individual trees are extracted for each neuron.*

We outline below a strategy for neuronal tracing that is designed to sort individual neuronal trees found in two-dimensional images where neurites from different neurons may overlap. This method relies critically on the soma segmentation method described above as it assigns the root of each neuronal tree corresponding to the soma location. The algorithm consists of the following steps:

1. *Segmentation and soma detection.* This is the algorithm presented in Sec. 3.4. It identifies somas and neurites.
2. *Path initialization.* It finds the initial location and orientation of each path emanating from a soma into a neurite.
3. *Tracing.* After generating seed points along the neurites using an appro-

priate distance function, it progressively compute paths along each neurite emanating from each soma. Intersecting neurites are solved by following the path with minimal change in orientation.

The application of this method to compute individual trees for each neuron in an image of a neuronal culture is illustrated in Fig. 6, showing that neuronal trees are accurately separated. The numerical code to generate this image is available at `https://github.com/cihanbilge/AutomatedTreeStructureExtraction`.

By computing separate traces for each neuron, this algorithm facilitates the computation of multiple morphometric characteristics corresponding to each neuron in the image. One main advantage of this approach is that each neurotic trace provides a local coordinate system that is useful to measure local expression levels of analytes visualized in the fluorescent image by computing their local intensity. A more detailed description and illustration of this algorithm is beyond the scope of this paper and will be discussed in future work.

Acknowledgements

D.L. acknowledges support from GEAR 113491, the Simon foundation (422488) and NSF-DMS 1720487 and 1720452.

References

[1] G. A. Ascoli, D. E. Donohue, M. Halavi, Neuromorpho.org: A central resource for neuronal morphologies, Journal of Neuroscience 27 (35) (2007) 9247–9251. doi:10.1523/JNEUROSCI.2055-07.2007.

[2] K. Brown, G. Barrionuevo, A. Canty, V. Paola, J. Hirsch, G. Jefferis, J. Lu, M. Snippe, I. Sugihara, G. Ascoli, The DIADEM data sets: representative light microscopy images of neuronal morphology to advance automation of digital reconstructions, Neuroinformatics 9 (2-3) (2011) 143–157.

[3] Y. Liu, The DIADEM and beyond, Neuroinformatics 9 (2-3) (2011) 99–102.

[4] R. Parekh, G. A. Ascoli, Neuronal morphology goes digital: a research hub for cellular and system neuroscience, Neuron 77 (6) (2013) 1017–1038. doi:10.1016/j.neuron.2013.03.008.

[5] H. Peng, B. Roysam, G. A. Ascoli, Automated image computing reshapes computational neuroscience, BMC Bioinformatics 14 (1) (2013) 293. doi:10.1186/1471-2105-14-293.

[6] H. Peng, E. Meijering, G. A. Ascoli, From DIADEM to bigneuron, Neuroinformatics 13 (3) (2015) 259–260. doi:10.1007/s12021-015-9270-9.

[7] C. Cortes, V. Vapnik, Support-vector networks, Mach. Learn. 20 (3) (1995) 273–297. doi:10.1023/A:1022627411411.

[8] G. Easley, D. Labate, W.-Q. Lim, Sparse directional image representations using the discrete shearlet transform, Applied and Computational Harmonic Analysis 25 (1) (2008) 25 – 46. doi:http://dx.doi.org/10.1016/j.acha.2007.09.003.

[9] D. Jimnez, D. Labate, I. Kakadiaris, M. Papadakis, Improved automatic centerline tracing for dendritic and axonal structures, Neuroinformatics 13 (2) (2015) 227–244. doi:10.1007/s12021-014-9256-z.

[10] B. Ozcan, P. Negi, F. Laezza, M. Papadakis, D. Labate, Automated detection of soma location and morphology in neuronal network cultures, PloS one 10 (4).

[11] E. J. Candes, D. L. Donoho, New tight frames of curvelets and optimal representations of objects with piecewise c2 singularities, Communications on Pure and Applied Mathematics 57 (2) (2004) 219–266. doi:10.1002/cpa.10116.

[12] G. Kutyniok, D. Labate, Shearlets: Multiscale Analysis for Multivariate Data, Springer, 2012.

[13] D. Labate, W. Lim, G. Kutyniok, G. Weiss, Sparse multidimensional representation using shearlets, SPIE Proc. 5914, SPIE, Bellingham (2005) 254–262.

[14] K. Guo, D. Labate, The construction of smooth Parseval frames of shearlets., Math. Model. Nat. Phenom. 8 (1) (2013) 82–105. doi:10.1051/mmnp/20138106.

[15] K. Guo, D. Labate, Optimally sparse multidimensional representation using shearlets, SIAM J. Math. Anal. 39 (1) (2007) 298–318.

[16] G. R. Easley, D. Labate, P. Negi, 3D data denoising using combined sparse dictionaries., Math. Model. Nat. Phenom. 8 (1) (2013) 60–74. doi:10.1051/mmnp/20138104.

[17] J.-L. Starck, E. J. Candes, D. L. Donoho, The curvelet transform for image denoising, Trans. Img. Proc. 11 (6) (2002) 670–684. doi:10.1109/TIP.2002.1014998.

[18] W.-Q. Lim, The discrete shearlet transform: A new directional transform and compactly supported shearlet frames, Trans. Img. Proc. 19 (5) (2010) 1166–1180. doi:10.1109/TIP.2010.2041410.

[19] P. Singh, P. S. Negi, F. Laezza, M. Papadakis, D. Labate, Multiscale analysis of neurite orientation and spatial organization in neuronal images, Neuroinformatics 14 (4) (2016) 465–477.

[20] D. Jimenez, D. Labate, I. A. Kakadiaris, E. Papadakis, Improved automatic centerline tracing for dendritic and axonal structures, Neuroinformatics 13 (2014) 227–244.

[21] J. B. Pawley, Handbook of biological confocal microscopy, Springer, New York (N.Y.), 2006.

[22] C. M. Weaver, J. D. Pinezich, W. B. Lindquist, M. E. Vazquez, An algorithm for neurite outgrowth reconstruction., J. Neurosci. Methods 124 (2003) 197–205.

[23] S. C. B. M. W. D. D. S. M. T. S. S. G. J. M. Vallotton P, Lagerstrom R, Automated analysis of neurite branching in cultured cortical neurons using hca-vision., Cytom.Part A 71 (10) (2007) 889–895.

[24] S. K. Schmitz, J. J. Hjorth, R. M. Joemai, R. Wijntjes, S. Eijgenraam, P. de Bruijn, C. Georgiou, A. P. de Jong, A. van Ooyen, M. Verhage, L. N. Cornelisse, R. F. Toonen, W. Veldkamp, Automated analysis of neuronal morphology, synapse number and synaptic recruitment, J Neurosci Methods 195 (2) (2011) 185–193. doi:10.1016/j.jneumeth.2010.12.011.

[25] C. B. Kayasandik, D. Labate, Improved detection of soma location and morphology in fluorescence microscopy images of neurons, Journal of Neuroscience Methods 274 (2016) 61–70. doi:10.1016/j.jneumeth.2016.09.007.

[26] G.-W. He, T.-Y. Wang, A.-S. Chiang, Y.-T. Ching, Soma detection in 3d images of neurons using machine learning technique, Neuroinformatics 16 (1) (2018) 31–41.

[27] D. Labate, F. Laezza, P. Negi, B. Ozcan, M. Papadakis, Efficient processing of fluorescence images using directional multiscale representations, Math. Model. Nat. Phenom. 9 (5) (2014) 177–193.

[28] N. Bannister, A. Larkman, Dendritic morphology of ca1 pyramidal neurones from the rat hippocampus: I. branching patterns, Journal of Comparative Neurology 360 (1) (1995) 150–160.

[29] J. C. Fiala, K. M. Harris, K. Spacek, Dendrite structure, Oxford University Press Oxford (UK), 1999.

[30] P. Perona, Steerable-scalable kernels for edge detection and junction analysis, Image Vision Comput. 10 (10) (1992) 663–672.

[31] J.-M. Geusebroek, A. Smeulders, J. van de Weijer, Fast anisotropic gauss filtering, IEEE Trans Image Process 12 (8) (2003) 938–943.

[32] A. Buades, B. Coll, J. Morel, A review of image denoising algorithms, with a new one, Multiscale Modeling & Simulation 4 (2) (2005) 490–530. doi:10.1137/040616024.

[33] J. A. Sethian, Level Set Methods and Fast Marching Methods., 2nd Edition, Cambridge University Press, 1999.

[34] T. Lindeberg, Feature detection with automatic scale selection, International Journal of Computer Vision 30 (2) (1998) 79–116.

[35] D. Jimenez, D. Labate, I. A. Kakadiaris, M. Papadakis, Improved automatic centerline tracing for dendritic and axonal structures, Neuroinformatics 13 (2014) 1–18. doi:10.1007/s12021-014-9256-z.

[36] P. C. S. W. T. J. e. a. Al-Kofahi Y, Dowell-Mesfin D, Improved detection of branching points in algorithms for automated neuron tracing from 3D confocal images., Cytom.Part A 73(1) (2008) 3643.

[37] P. Vallotton, R. Lagerstrom, C. Sun, M. Buckley, D. Wang, et al., Automated Analysis of Neurite Branching in Cultured Cortical Neurons Using HCA-Vision., Cytom. Part A 71 (10) (2007) 889–895.